https://doi.org/10.5194/wes-2026-111
Preprint. Discussion started: 22 July 2026

Bio-Inspired Outer-Span Hybridization of the NREL Phase VI Rotor for Enhancing Aerodynamic Performance and Flow-Field Stability

Yassine EL Qamch[1], Khaoula Qaissi[1], Ashraf A. Omar[1], Wafae Lahmili[1], Kenza Bouchaala[1,2]

[1]International University of Rabat – School of Aerospace and Automotive engineering – Parc Technopolis Rabat –Rocade de Rabat-Salé 11100 – Sala Al Jadida – Morocco
[2]Laboratory of Energy, Materials and Sustainable Development, ENSAM, Moulay Ismail University, 15290, Meknes, Morocco
Correspondence to: Ashraf A. Omar (ashraf_omar@uir.ac.ma)

Abstract. The presenting work evaluates a selective bio-inspired outer-span hybridization of the NREL Phase VI wind turbine rotor. An owl-inspired airfoil (OA-T), obtained through controlled thickness scaling of a reconstructed owl-wing section, is integrated over the outer 20% of the blade span while preserving the original chord and twist distributions. The objective is to assess whether localized geometric modification in the torque-dominant tip region can improve aerodynamic performance under increasing loading. A validated CFD framework is employed at both airfoil and rotor scales. Transition SST simulations reproduce the experimental lift behavior of the owl-inspired airfoil, while steady RANS–MRF simulations capture the torque response of the baseline Phase VI rotor. Using the same modeling setup, the hybrid configuration demonstrates a systematic increase in peak power coefficient from 0.38 to 0.42 at a tip speed ratior $\lambda = 5.41$, reaching 0.448 at higher tip-speed ratios. Flow-field analysis reveals outward redistribution of tangential loading, a shift toward a more chordwise-distributed pressure response, delayed separation progression, and a more confined wake structure at elevated wind speeds. The results show that controlled outer-span hybridization within a benchmark rotor can enhance torque retention and aerodynamic stability without full-blade redesign.

Keywords: Bio-inspired airfoil, NREL Phase VI, Wind turbine aerodynamics; CFD validation, Power coefficient; Tip-vortex dynamics.

Nomenclature

r — Radial position along blade (m)

R — Rotor radius (m)

c — Chord length (m)

t/c — Thickness-to-chord ratio

U_∞ — Free-stream velocity ($m \cdot s^{-1}$)

ρ — Fluid density ($kg \cdot m^{-3}$)

ν — Kinematic viscosity ($m^2 \cdot s^{-1}$)

P — Static pressure (Pa)

T — Rotor shaft torque (N·m)

P shaft — Shaft power (W)

C_L — Lift coefficient

C_D— Drag coefficient

https://doi.org/10.5194/wes-2026-111
Preprint. Discussion started: 22 July 2026

Cp — Pressure coefficient

C_P — Power coefficient

C_T — Tangential force coefficient

x/c — Normalized chordwise coordinate

α — Angle of attack (deg)

λ — Tip-speed ratio

Abbreviations

CFD — Computational Fluid Dynamics

RANS — Reynolds-Averaged Navier–Stokes

URANS — Unsteady Reynolds-Averaged Navier–Stokes

SST — Shear Stress Transport

MRF — Multiple Reference Frame

TKE — Turbulent Kinetic Energy

LSB — Laminar Separation Bubble

OA-T — Thickness-modified owl-inspired airfoil

HAWT — Horizontal-Axis Wind Turbine

https://doi.org/10.5194/wes-2026-111
Preprint. Discussion started: 22 July 2026

1. Introduction:

The continuous growth of wind energy deployment has intensified the need for aerodynamic optimization strategies capable of improving energy capture while maintaining stable operation across a wide range of inflow conditions. For horizontal-axis wind turbines (HAWTs), aerodynamic performance is governed not only by the two-dimensional characteristics of individual airfoils but also by three-dimensional flow effects, rotational augmentation, stall progression, and tip-vortex dynamics (Burton et al., 2011; Hansen, 2015; Sørensen, 2011). Among the blade regions, the outer span is of particular importance because it contributes disproportionately to rotor torque due to its larger local tangential velocity and longer aerodynamic moment arm (Aldheeb et al., 2016), (Anyoji et al., 2018). However, this region is also highly sensitive to adverse pressure gradients, three-dimensional separation, and vortex-induced losses, especially under moderate-to-high wind speeds where stall development may initiate near the tip Aono et al. (2020),(Du and Selig, 1998),(Johansen and Sørensen, 2004).

These investigations have provided clearer insight into the interaction between sectional airfoil behavior and global rotor performance. Previous studies have shown that modifying the spanwise distribution of aerodynamic loading can significantly influence stall behavior, tip-vortex intensity, and overall rotor efficiency (Omar et al., 2023),(Qamch et al., 2026). In this context, localized geometric modifications of the outer blade region present an attractive strategy, as they allow targeted aerodynamic improvement without requiring complete rotor redesign. However, such modifications must be approached carefully. Excessive front-loading near the leading edge or overly aggressive camber variations may increase sensitivity to separation and lead to undesirable wake development (Anyoji et al., 2018). Consequently, geometric modifications must be evaluated not only in terms of lift enhancement, but also with respect to flow stability, power output, and wake organization.

Bio-inspired aerodynamic concepts have gained attention in both aerospace and wind-energy research, particularly drawing inspiration from avian flight mechanisms (Aldheeb et al., 2016; El Qamch et al., 2025; Howe, 1991; Jaworski and Peake, 2013), (Omar et al., 2020). In the context of owls, specific attention has been directed toward trailing-edge serrations and surface features associated with silent flight and boundary-layer control (Geyer et al., 2010; Lahmili et al., 2026; Qaissi et al., 2023). At the airfoil level, owl-inspired geometries have been studied at low Reynolds numbers to understand laminar separation bubble dynamics and transition sensitivity (Aono et al., 2020), (Boughou et al., 2023),(Ashraf et al., 6-9 june) . More broadly, bio-inspired airfoils and wing configurations have been shown to offer promising aerodynamic behavior in low-Reynolds-number regimes, particularly in terms of flow control and separation mitigation. However, most of these studies remain limited to two-dimensional or isolated configurations, and their direct application to rotating wind turbine blades remains insufficiently explored. In particular, the systematic evaluation of selective outer-span hybridization using bio-inspired airfoils within a consistent rotor framework has not been widely reported. While existing work has provided valuable insight into airfoil-level performance and global rotor modeling strategies, fewer studies have investigated how localized geometric substitution in the torque-dominant region influences spanwise load redistribution and rotor-scale aerodynamic behavior. Rather than proposing a fully bio-inspired rotor architecture, this study adopts a controlled and incremental approach based on selective outer-span hybridization. An owl-inspired airfoil (OA-T) (A. Omar et al., 2020) is integrated into the outer span of the blade while preserving the baseline configuration elsewhere. This strategy allows the geometric effect of the modified airfoil to be isolated from other design variables and avoids the need for full-blade redesign. The motivation for this approach is twofold. First, the outer-span region dominates torque production (**Fig. 1**), and modest improvements in sectional pressure distribution may translate into measurable gains in global performance (Burton et al., 2011; Hansen, 2015). Second, as wind speed increases, this region becomes increasingly susceptible to separation and tip-induced flow distortion. A geometry capable of redistributing chordwise pressure loading more evenly may contribute to improved flow organization and sustained torque generation under higher loading conditions.

https://doi.org/10.5194/wes-2026-111
Preprint. Discussion started: 22 July 2026

eawe european academy of wind energy
Open Access WIND ENERGY SCIENCE DISCUSSIONS

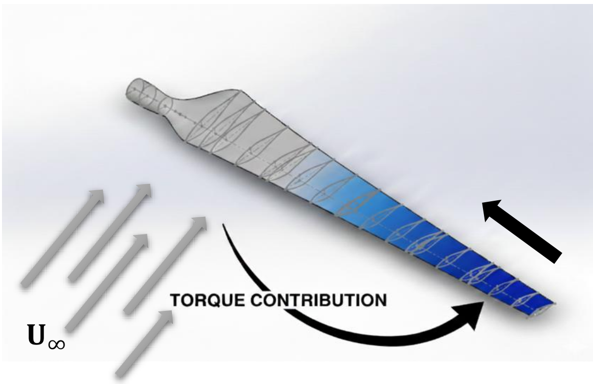

Figure. 1 Torque contribution profile along the rotor blade span

To evaluate this hypothesis, a validated CFD framework is employed at both airfoil and rotor scales. The owl-inspired airfoil behavior is first assessed against available experimental data to ensure adequate representation of low-Reynolds-number flow mechanisms. Within this context, the present work aims to assess how targeted outer-span airfoil substitution influences aerodynamic performance and flow-field behavior at the rotor scale. The objective is to clarify the relationship between sectional geometric modification, spanwise load redistribution, and wake development under increasing wind-speed conditions. Although the analysis is conducted within a well-established reference configuration, the underlying aerodynamic mechanisms associated with outer-span loading and tip-region sensitivity are common to horizontal-axis wind turbines more broadly (Aldheeb et al., 2016), Aono et al. (2020). Consequently, the present approach should be interpreted not as a redesign limited to a single reference rotor, but as a controlled investigation of how targeted outer-span airfoil substitution may enhance aerodynamic stability and torque retention in HAWTs more broadly, without requiring full-blade geometric reconfiguration. A preliminary version of this work was presented at the TORQUE 2026 conference (Qamch et al., 2026). The present manuscript substantially extends that contribution by introducing additional three-dimensional simulations, expanded outer-span flow analyses, and new physical interpretation of pressure redistribution, wake development, and torque retention that were not included in the conference publication.

2. Methodology:

2.1. Airfoil Geometry and Numerical Setup

2.1.1. Owl-Inspired Airfoil Definition

The baseline owl-inspired airfoil employed in this study originates from a bio-inspired reconstruction of an owl wing cross-section extracted at approximately 40% of the wing span, following the geometric characterization reported by Liu et al. (Liu et al., 2006). The objective of this reconstruction is not to replicate the biological geometry exactly, but to reproduce the key aerodynamic features associated with owl wings, particularly those linked to low-Reynolds-number flight. The resulting baseline airfoil, shown in **Fig.2** (a), is characterized by a relatively flat upper surface, a thin trailing edge, and a camber distribution concentrated toward the mid-chord region. The maximum thickness of the baseline profile is 5.66% of the chord, located at $x/c=0.11$ (11%), while the peak camber reaches 4.83% of the chord at $x/c=0.48$. These geometric characteristics are consistent with smooth pressure recovery behavior and streamlined profiles typically reported for owl-inspired sections. To ensure structural compatibility with wind-turbine blade integration while preserving the original camber distribution, a controlled thickness-scaling transformation was applied about the camber line (Eq.1). The chord was normalized to unity, and the camber line was defined as the mean line between upper and lower surfaces at each chordwise location. Each surface coordinate was transformed according to

https://doi.org/10.5194/wes-2026-111
Preprint. Discussion started: 22 July 2026

WIND ENERGY SCIENCE DISCUSSIONS

$$y_{new} = y_{camber} + (y_i - y_{camber}) \times S \qquad (1)$$

where S represents the ratio between the target and baseline thickness, y_i original y coordinate, and y_{camber} the y coordinate of the camber line at the same x location

The resulting modified airfoil, denoted OA-T (**Fig.2** (bottom)), preserves the camber-line characteristics and overall curvature of the baseline geometry while increasing the maximum thickness-to-chord ratio to 0.115. The maximum thickness location remains near the leading-edge region (x/c≈0.11), ensuring geometric continuity with the baseline shape. The detailed geometric derivation and validation of the owl-inspired airfoil are provided in (El Qamch Yassine et al., 2025); in the present study, only the OA-T configuration is retained for rotor hybridization.

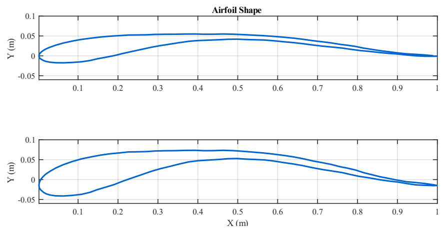

Figure. 2 Coplot of (*Top*) owl airfoil, (*Bottom*) OA-T airfoil

2.1.2. Airfoil-Level CFD Configuration

The aerodynamic behavior of the baseline owl airfoil and the OA-T configuration was evaluated using two-dimensional Reynolds-Averaged Navier–Stokes (RANS) simulations with a finite-volume, pressure-based solver under incompressible flow conditions. The governing equations correspond to the time-averaged conservation equations of mass and momentum throught reynold decomposition(Eq 2-4):

$$\mathrm{ui} = \mathrm{ui} + \mathrm{ui}', \mathrm{p} = \mathrm{p} + \mathrm{p}' \qquad (2)$$

$$\nabla \cdot \mathrm{U} = 0 \qquad (3)$$

$$\rho(\mathrm{U} \cdot \nabla)\mathrm{U} = -\nabla \mathrm{p} + \mu \nabla^2 \mathrm{U} - \rho \nabla \cdot \overline{\mathrm{ui}'\mathrm{uj}'} \qquad (4)$$

Second-order spatial discretization schemes were applied to the momentum and turbulence equations to ensure accurate resolution of pressure gradients and boundary-layer development. Two turbulence modeling approaches were employed. The *k–ω* SST model was first used to accurately capture adverse pressure gradients and flow separation typical of airfoil aerodynamics. The model solves two transport equations for the turbulent kinetic energy k (Eq 5) and the specific dissipation rate ω (Eq 6):

$$\partial(\rho k)/\partial t + \partial(\rho U_j k)/\partial x_j = P_k - \beta * \rho k \omega + \partial/\partial x_j[(\mu + \sigma_k \mu_t)\partial k/\partial x_j] \qquad (5)$$

$$\partial(\rho\omega)/\partial t + \partial(\rho U_j \omega)/\partial x_j = \alpha \left(\frac{\omega}{k}\right) P_k - \beta\rho\omega^2 + \partial[(\mu + \sigma_\omega \mu_t)\partial\omega/\partial x_j]/\partial x_j + 2(1 - F^1)\rho\sigma_\omega 2(1/\omega)(\partial k/\partial x_j)(\partial\omega/\partial x_j) \qquad (6)$$

To capture laminar–turbulent transition and laminar separation bubble behavior typical of low-Reynolds-number flows, the Transition *SST* (γ–Reθ) model was additionally employed. This model augments the SST formulation with two transport equations for the intermittency γ and the transition momentum thickness Reynolds number Re_θ (Eq 7-8):

https://doi.org/10.5194/wes-2026-111
Preprint. Discussion started: 22 July 2026

$$\partial(\rho\gamma)/\partial t + \partial(\rho U_j\gamma)/\partial x_j = P_\gamma - E_\gamma + \partial/\partial x_j[(\mu + \sigma_f\mu_t)\partial\gamma/\partial x_j] \quad (7)$$

$$\partial(\rho Re_\theta)/\partial t + \partial(\rho U_j Re_\theta)/\partial x_j = P_\theta + \partial/\partial x_j[\sigma_\theta(\mu + \mu_t)\partial Re_\theta/\partial x_j] \quad (8)$$

A structured C-type computational domain was generated around each airfoil section (**Fig.3**). Mesh refinement was applied along the airfoil surface and in the near-wake region. The near-wall resolution was selected to maintain $y^+ < 1$ along the surface, consistent with *SST*-based turbulence and transition modeling requirements. Uniform velocity inlet and pressure outlet boundary conditions were prescribed, while far-field boundaries were treated as symmetry planes. A no-slip condition was imposed at the airfoil surface.

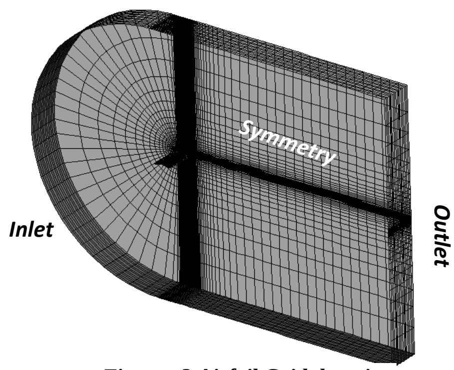

Figure. 3 Airfoil Grid domain

Grid independence was assessed using four progressively refined meshes, summarized in Table 1. Aerodynamic coefficients were compared at a representative angle of attack of 10°. At this angle of attack, stronger pressure gradients and boundary-layer development occur, making the solution more sensitive to mesh resolution. Differences between the selected mesh and the next finer grid were below 0.5% for lift and 1% for drag, indicating sufficient spatial convergence (The agreement with experimental data is assessed separately in the validation section). The corresponding mesh (267,860 elements) was therefore retained for all subsequent airfoil simulations.

Table 1. Grid resolution impact on time dependent Lift Coefficient values at angle 10°

Mesh resolution	Number of Elements	Lift Coefficient (C_l)	ΔC_l (%)	Drag Coefficient (C_d)	ΔC_d (%)
Coarse	86413	1.051	2.23	0.0990	6.56
Medium	154194	1.075	0.18	0.0929	0.97
Fine 1	267860	1.073	0.46	0.0920	0.32
Fine 2	690209	1.073	___	0.0920	___

2.1.3. Rotor-Level CFD Configuration

https://doi.org/10.5194/wes-2026-111
Preprint. Discussion started: 22 July 2026

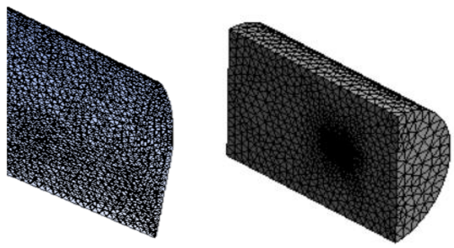

Figure. 4 Computational Grid of the NREL Phase VI Rotor (Half-Domain, MRF Configuration)

Three-dimensional simulations of the baseline NREL Phase VI rotor and the Hybrid Model A configuration were performed using a steady Reynolds-Averaged Navier–Stokes (RANS) approach. The rotor rotation was modeled using a Multiple Reference Frame

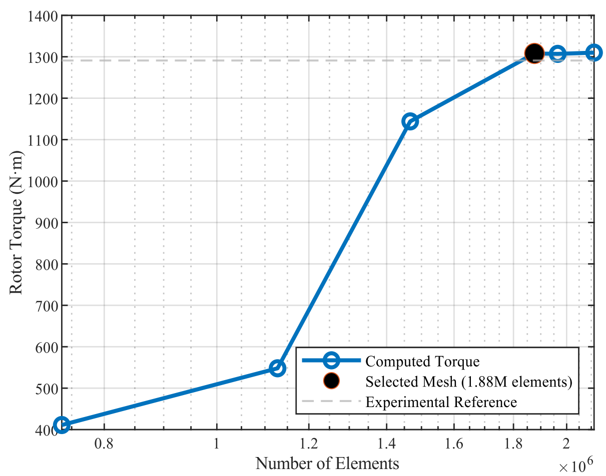

Figure. 5 Rotor Torque Convergence against experimental data (Lahmili et al., 2026) with Mesh Refinement (Grid Independence Study)

(MRF) formulation at a fixed rotational speed of 72 rpm. To reduce computational cost while preserving rotational periodicity, a half-rotor computational domain was employed, with periodic boundary conditions imposed on the azimuthal planes (**Fig.4**). A uniform velocity inlet was prescribed upstream of the rotor, and a pressure outlet (0 Pa gauge) was imposed downstream. Blade surfaces were treated as no-slip walls. The k–ω SST turbulence model was adopted for all rotor simulations due to its robustness in resolving adverse pressure gradients and separation phenomena typical of wind-turbine blade operation (Menter, 1994; Rocha et al., 2014). Near-wall mesh resolution was selected to maintain $y^+ < 1$ over the blade surface, ensuring accurate boundary-layer resolution. The rotor mesh is unstructured tetrahedral mesh, that was generated with local refinement along the blade surfaces and in the near-wake region. A minimum surface element size of 0.01 m was used on the blade, and the selected operating mesh contained 1.8 M elements. Second-order spatial discretization schemes were applied for the momentum equations. Convergence was assessed through residual reduction and stabilization of integrated rotor quantities, particularly shaft torque. To verify mesh independence, a grid convergence study was conducted at an inflow velocity of 10 m/s. Six progressively refined meshes, ranging from 0.73 million to 2.11 million elements, were evaluated using rotor shaft torque as the convergence metric (**Fig.5**). While substantial variation is observed for the two coarsest grids, the solution stabilizes beyond approximately 1.47 million elements. The

https://doi.org/10.5194/wes-2026-111
Preprint. Discussion started: 22 July 2026

selected mesh (1.876 million elements) lies within this convergence plateau region. The torque variation between the selected mesh and the two finer grids remains below 0.3%, indicating mesh-independent behavior. Further refinement yields negligible changes in integrated torque while significantly increasing computational cost. This mesh was therefore retained for all baseline and hybrid rotor simulations.

2.1.4. Hybridization and Blade Geometry Implementation

The baseline rotor geometry corresponds to the NREL Phase VI blade (Burton et al., 2011), which has been extensively used as a benchmark configuration for aerodynamic validation and stall investigations due to its well-documented geometry and the availability of high-quality wind-tunnel measurements. This makes it particularly suitable as a reference case for evaluating the aerodynamic impact of localized geometric modifications under controlled and comparable conditions. The chord and twist distributions of the blade are defined as a function of radial position (see Appendix D), and the reference geometry was reconstructed in SolidWorks using the published spanwise stations (Burton et al., 2011), preserving the original chord length, twist angle, and twist-axis definition along the span. To isolate the aerodynamic impact of the bio-inspired modification, the hybrid configuration was generated by replacing the airfoil sections over the outer 20% of the blade span ($r/R \geq 0.80$) with the OA-T profile while maintaining the original chord, twist, and radial placement. No changes were introduced to the inboard and mid-span sections, ensuring that the structural layout and global blade planform remained identical to the baseline configuration. This approach allows a direct comparison between the baseline and modified configurations, where any observed differences can be attributed solely to the introduced airfoil substitution. The decision to restrict the modification to the last 20% of the span follows classical rotor aerodynamics principles: the outer blade region contributes disproportionately to torque production due to its larger tangential velocity and aerodynamic moment arm (Aldheeb et al., 2016),(Anyoji et al., 2018), while also being the region most sensitive to three-dimensional separation and tip-vortex development under elevated loading Aono et al. (2020),(Boughou et al., 2023). By limiting the hybridization to this region, the geometric intervention remains controlled and localized, allowing the influence of the OA-T airfoil on spanwise load redistribution and wake organization to be assessed without introducing full-blade redesign effects. **Fig.6** illustrates the baseline and Hybrid Model A geometries, highlighting the outer-span replacement region. Detailed blade geometric parameters used for reconstruction are provided in Appendix D.

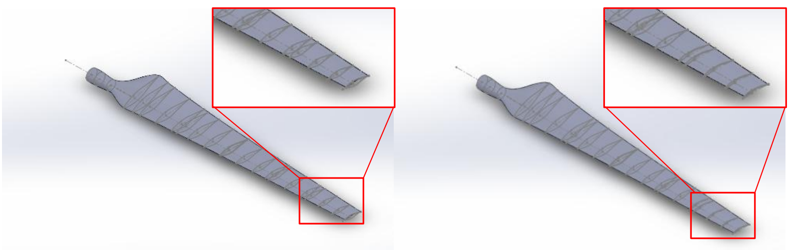

Figure. 6 Baseline (left) and hybrid Model A geometry (right)

3. Results and Discussion

3.1. Model Validation

3.1.1. Sectional airfoil validation

https://doi.org/10.5194/wes-2026-111
Preprint. Discussion started: 22 July 2026

Before evaluating the aerodynamic performance of the proposed owl-inspired rotor, the numerical framework is first validated at the airfoil level. The validation focuses on the lift coefficient variation with angle of attack, $C_L(\alpha)$. **Fig.7** compares the lift

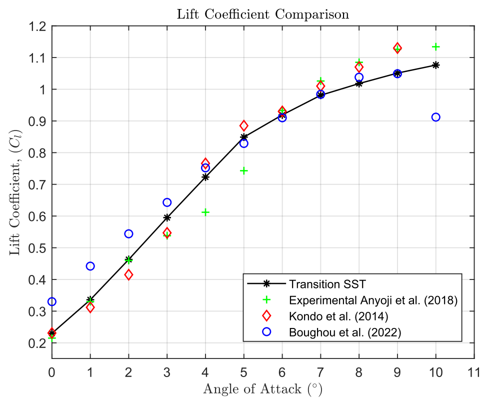

Figure. 7 Comparison of Lift Coefficient Predictions for Owl Airfoil Using Numerical Models and Experimental Data

coefficient predicted using the Transition SST model with experimental measurements from Anyoji *et al*. (Anyoji et al., 2018) and selected CFD literature data (Boughou et al., 2023; Kondo et al., 2014). The numerical results reproduce the overall lift-curve shape and slope. The linear increase in lift at low angles of attack, governed by attached-flow behavior, is well predicted. The model also reproduces the nonlinear aerodynamic behavior at moderate angles of attack. Predicted lift levels remain close to the experimental trend over the investigated range, indicating that the dominant low-Reynolds-number flow mechanisms are well captured. A localized deviation is observed in the intermediate range $\alpha \approx 4^{\circ}$- 6°, where the numerical lift is slightly lower than the experimental values. This region corresponds to a nonlinear lift-increase regime explicitly reported by (Anyoji *et al.* ; Qamch, Omar, et al., 2026)

, who associated it with the formation and evolution of a laminar separation bubble. Their analysis showed that, around $\alpha \approx 5°$, the separation bubble switches from the pressure side to the suction side, making the lift coefficient highly sensitive to transition and reattachment location. Such sensitivity is known to challenge RANS-based transition models and commonly leads to small discrepancies in this angle-of-attack range. Additional differences may arise from experimental factors, including the finite trailing-edge thickness of the tested airfoil and minor geometric deviations from an idealized profile. Despite these localized offsets, the numerical model manages to capture the experimentally observed nonlinear trend, and the global lift behavior. The agreement is therefore considered sufficient for rotor-level comparative studies using the same aerodynamic modeling approach.

3.1.2. Rotor-level validation: NREL Phase VI torque response

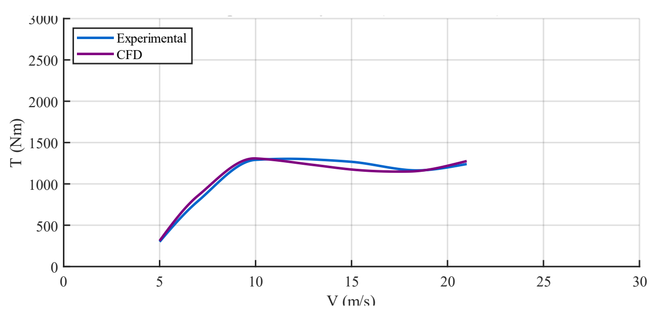

Figure. 8 Comparison of Lift Coefficient Predictions for Owl Airfoil Using Numerical Models and Experimental Data (Lahmili et al., 2026)

https://doi.org/10.5194/wes-2026-111
Preprint. Discussion started: 22 July 2026

Following the airfoil-level assessment, the numerical framework is further validated at the rotor level using the well-documented NREL Phase VI horizontal-axis wind turbine. Simulations were performed at the experimental rotational speed of 72 rpm over the wind-speed range investigated in the NREL Phase VI campaign. Rotor shaft torque is selected as the validation metric because it reflects the integrated aerodynamic loading over the blade span and is particularly sensitive to transition effects and stall development. **Fig. 8** compares the numerically predicted torque with experimental measurements (Lahmili et al., 2026) as a function of inflow wind speed for the baseline Phase VI configuration. The numerical results closely follow the experimental trend across the investigated operating range. The model accurately captures the rapid increase in torque at low wind speeds, corresponding to predominantly attached flow conditions. As the wind speed increases further, the torque trend is well predicted as stall progressively develops along the blade. Small discrepancies are observed near the transition between attached and stalled regimes, where rotor torque is known to be sensitive to three-dimensional separation, blade–wake interaction, and transition modeling. Nevertheless, the numerical framework reproduces both the magnitude and location of the torque peak, as well as the overall torque–velocity relationship.

At this level of agreement, we can say that the numerical approach is capable of predicting integrated rotor performance with sufficient accuracy. The same modeling strategy is therefore retained unchanged to evaluate the aerodynamic impact of introducing the owl-inspired OA-T airfoil in the outer blade region.

3.2. Performance Comparison of the Baseline blade and the hybrid blade

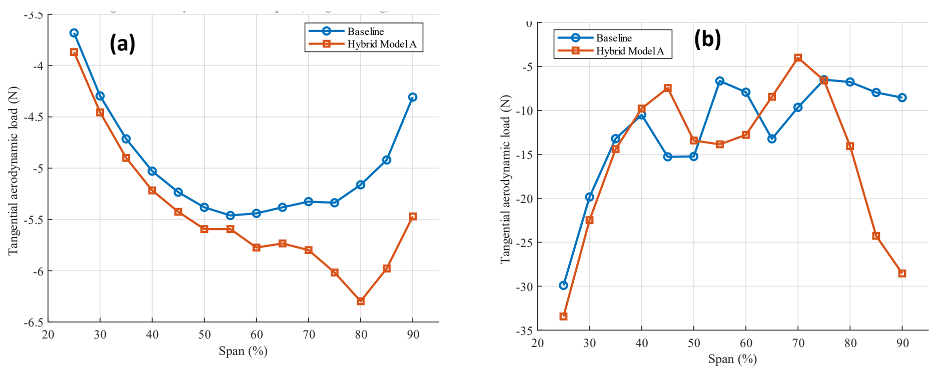

Figure. 9 Spanwise distribution of tangential aerodynamic load for the baseline and Hybrid Model A rotors at 72 rpm, (a) 5 m/s and (b) 15m/s

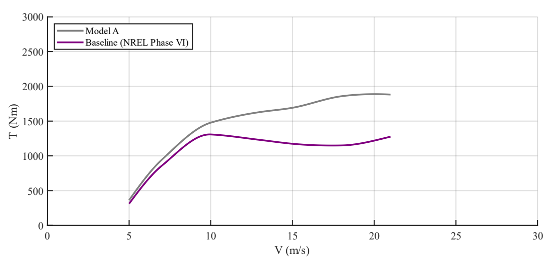

Fig. 10 Torque vs Velocity Curve (NREL Phase VI)

https://doi.org/10.5194/wes-2026-111
Preprint. Discussion started: 22 July 2026

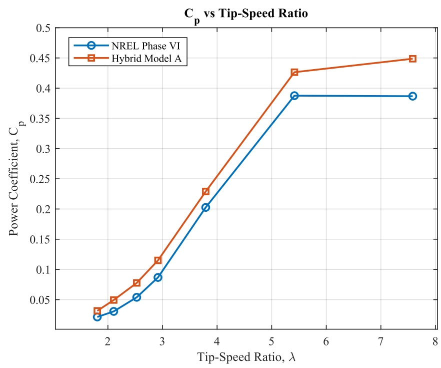

Fig. 11 Cp Vs TSR comparison of NREL Phase VI and the hybrid Model A rotors at fixed rotational speed of 72 rpm

This aerodynamic performance of the baseline NREL Phase VI rotor is compared with the hybrid Model. A blade configuration to assess the impact of the outer-span airfoil modification on rotor power extraction. The comparison is made through both local and global analyses. The spanwise distributions of tangential aerodynamic load (**Fig. 9**) illustrate how the aerodynamic torque is generated and redistributed along the blade span at 5 m/s and 15 m/s, as relevant cases for attached-flow-dominated and separated-flow-dominated conditions—note that as the blade is rotating counterclockwise (CCW) and the incoming flow is $-z$ directed, the aerodynamic load opposes the CCW direction by convention—while the global power coefficient and shaft power characteristics (**Fig. 11** and **12**) quantify the integrated effect of these local changes. This redistribution of spanwise aerodynamic loading translates directly into higher rotor torque, as confirmed by the torque–wind-speed comparison shown in **Fig.10**. Figure 10 compares the rotor torque predicted for the baseline and Hybrid Model A configurations over the investigated wind-speed range. Both rotors exhibit the expected increase in torque at low wind speeds under predominantly attached-flow conditions. The hybrid configuration produces slightly higher torque across most of the operating range. The difference becomes more noticeable at moderate and higher wind speeds indicating that the outer-span OA-T modification improves the aerodynamic loading distribution in the torque-producing region of the blade.

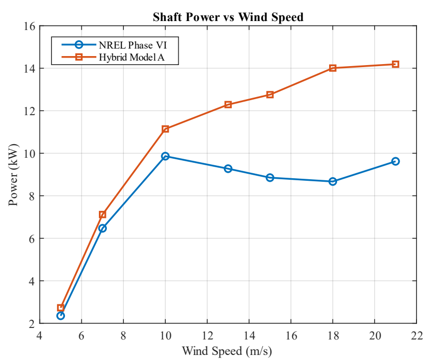

Fig. 12 Shaft Power Vs Wind speed comparison of NREL Phase VI and the hybrid Model A rotors at fixed rotational speed of 72 rpm

At 5 m/s, both rotors display the typical NREL Phase VI spanwise loading distribution, with tangential loads gradually increasing from the root toward the mid-span and then declining slightly near the tip due to reduced effective inflow and tip-vortex effects (**Fig. 9.a**). The Hybrid Model A exhibits a moderate increase in tangential aerodynamic load from 60 % up to about 80 % span, after which the load gradually decreases toward the tip (**Fig.9.a**) reaching a peak of 1.1 N in tangential force difference between the

https://doi.org/10.5194/wes-2026-111
Preprint. Discussion started: 22 July 2026

generated loadings at 80% span. This trend corresponds to the region where the OA-T airfoil modification (80–100 % span) becomes dominant. The OA-T section's thicker and more curved profile enhances local suction and circulation while promoting a smoother pressure recovery near the tip. The resulting aerodynamic behavior produces a stronger yet more stable load distribution, achieving higher torque without excessive tip over-loading—consistent with the intended goal of improving aerodynamic efficiency while mitigating vortex-induced losses. This is consistent with the observed torque improvement of the OA-T rotor in the low-speed region.

At 15 m/s as shown in Fig. 9.b, the aerodynamic loading intensifies along the entire span due to higher dynamic pressure, and both curves display load variations associated with local stall and reattachment phenomena, with markedly stronger fluctuations observed for the baseline rotor. The baseline rotor shows irregular peaks between 50 % and 70 % span, indicating partial stall propagation along the outer sections. In contrast, the Hybrid Model A maintains a more uniform load distribution toward the outer span, with a pronounced load peak around 70 % span followed by a smoother unloading toward the tip, where the OA-T airfoil mitigates stall and sustains lift under higher inflow angles. In this region, the difference of generated loading between the Hybrid Model A and the baseline reaches approximately **7 N**. this difference occurs contributes disproportionately to the integrated rotor torque and helps explain the higher torque levels predicted for Hybrid Model A at elevated wind speeds.

These local trends are consistent with the global aerodynamic results shown in the Cp–TSR and Shaft Power–Velocity curves (Fig 11 and 12, respectively). The baseline NREL Phase VI rotor reaches a peak power coefficient of C_p=0.38 at λ=5.41, maintaining that level up to λ=7.58. In contrast, the Hybrid Model A achieves C_p=0.42 at λ=5.41 and rises further to C_p=0.448 at λ=7.58, representing a 7–10 % increase in aerodynamic efficiency across the optimal operating range. This improvement reflects the local load intensification observed on the modified tip region and the reduced flow separation evidenced at high wind speeds. In addition to that, the shaft-power evolution confirms that the Hybrid Model A sustains higher torque and power output throughout the operating envelope. The baseline rotor's power saturates around 10 kW beyond 10 m/s due to flow separation and tip losses, whereas the Hybrid Model A continues to increase up to ≈14 kW near 18 m/s, highlighting improved aerodynamic stability and energy conversion capability. The enhanced performance can be attributed to the OA-T airfoil's higher lift-to-drag ratio, smoother pressure recovery, and improved stall resistance at the outer blade section. With that being said, the integration of the owl-inspired OA-T airfoil in the outer portion of the blade effectively shifts the torque-producing region outward, increasing aerodynamic efficiency and moderating tip-vortex intensity. The combined local and global results confirm that the Hybrid Model A delivers a balanced improvement in both global power extraction and local aerodynamic behavior.

3.3. Flow-field analysis of OA-T modification

The Hybrid Model A demonstrated improved global performance, with a noticeable increase in torque and, consequently, enhanced power generation compared to the baseline configuration. To better understand the origin of this improvement, the aerodynamic mechanisms responsible for this behavior are analyzed. The local flow characteristics, governing blade loading and flow development along the span, are compared are representative conditions**. Fig. 13 and 14** compares the sectional velocity streamlines around the baseline NREL Phase VI blade and the hybrid model A blade at 5 and 15 m/s, extracted at spanwise locations of 70 %, 75 %, 85 %, and 95 %. These locations cover the transition from the unmodified mid-span region to the OA-T-modified outer blade and the near-tip zone. At 5 m/s, the flow remains predominantly attached for both blade configurations across all investigated spanwise sections. The streamline patterns show smooth alignment over the suction surface and no evidence of large-scale separation or recirculation, which is consistent with operation at low effective angles of attack and low dynamic pressure. As a result, the baseline and hybrid model A exhibit similar flow organization at this wind speed, explaining why both rotors deliver comparable torque levels under attached-flow-dominated conditions.

https://doi.org/10.5194/wes-2026-111
Preprint. Discussion started: 22 July 2026

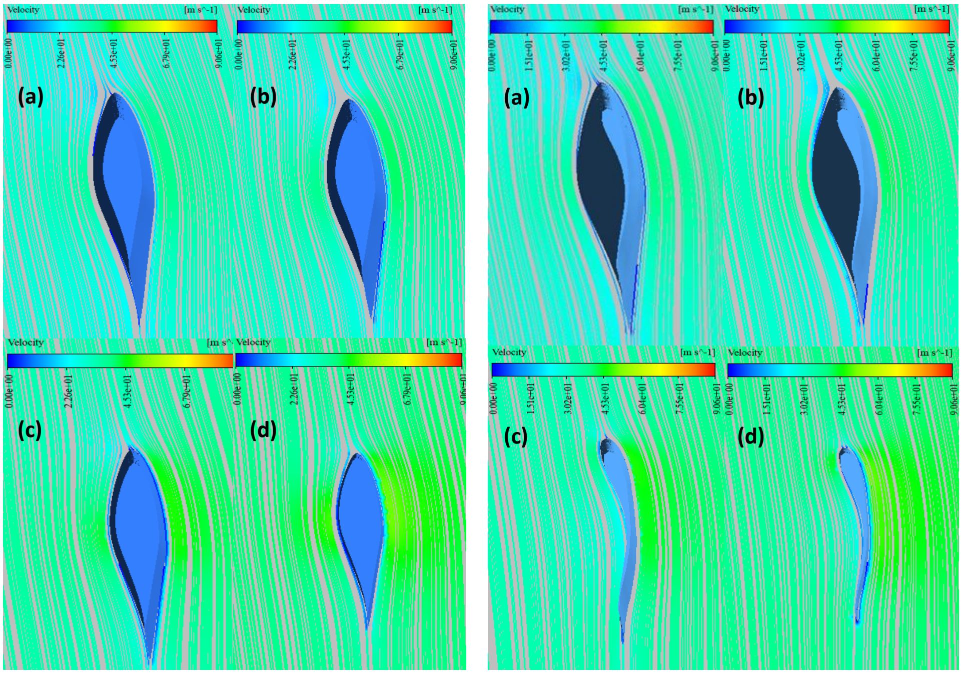

Fig. 13 Velocity streamlines around the NREL Phase VI blade (left) and the Hybrid Model A blade (right) at 5 m/s at locations (a)70%, (b)75%, (c)85%, d (95%) span

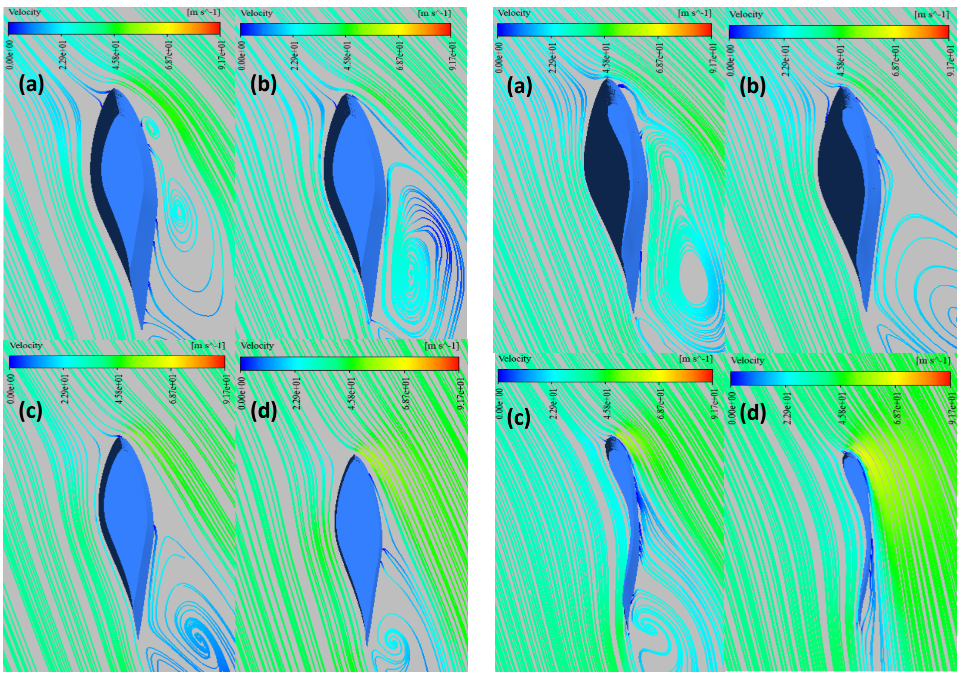

Figure. 14 Velocity streamlines around the NREL Phase VI blade (left) and the Hybrid Model A (right) at 15m/s at locations (a)70%, (b)75%, (c)85%, d (95%) span

In this regime, the OA-T modification does not fundamentally alter the flow topology but sustains attached flow toward the outer span without introducing additional losses. At intermediate wind speeds, the evolution of the flow field highlights the

https://doi.org/10.5194/wes-2026-111
Preprint. Discussion started: 22 July 2026

progressive onset of separation effects and clarifies the role of the OA-T modification. Velocity streamlines at 10 m/s and 13 m/s, examined at 90 % span (**Fig 15**), reveal the early stages of flow separation for the baseline blade. At 10 m/s, the baseline configuration shows the onset of separation on the pressure side beginning at approximately 65 % of the local chord from the leading edge, while the hybrid model A maintains attached flow further downstream, with separation delayed to around 75 % chord. As the wind speed increases to 13 m/s, separation for the baseline blade advances further upstream, appearing before mid-chord, accompanied by a thicker wake and more pronounced recirculation. In contrast, the Hybrid Model A continues to sustain attached flow until approximately 55–60 % chord, with a noticeably smaller wake area. These intermediate cases illustrate a clear trend: the OA-T modification systematically delays separation onset and limits wake growth as aerodynamic loading increases, bridging the attached-flow behavior observed at 5 m/s and the more strongly separated regime observed at 15 m/s.

In contrast, at 15 m/s, we notice differences between the two designs. For the baseline blade, the outer-span sections (70–85 % span) exhibit a broadened wake region, increased streamline curvature, and localized recirculation structures near the suction side and trailing-edge region, indicating flow separation and partial stall development. These features become more pronounced toward the tip (95 % span), where the wake becomes more compact yet more energetic, and the increased streamline curvature and localized recirculation reflect the combined effects of higher effective inflow angles, adverse pressure gradients, and three-dimensional tip-

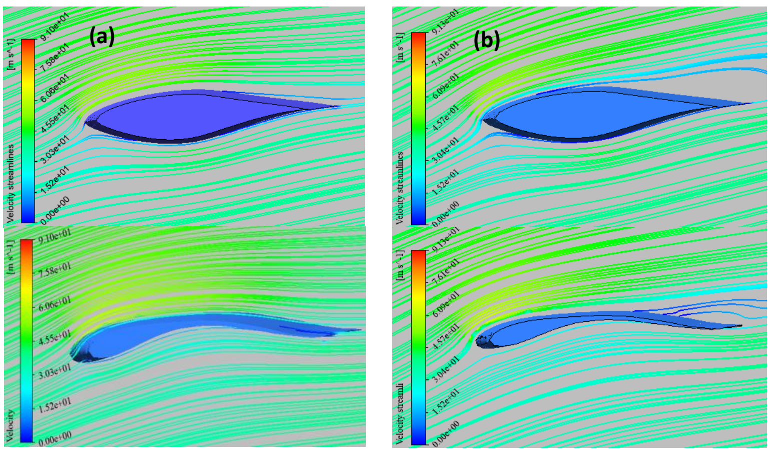

Figure 15 Sectional velocity streamlines at 90 % span for the baseline blade (top) and Hybrid Model A blade (bottom) at (a) 10 m/s and (b) 13 m/s, highlighting the evolution of separation and wake development.

region flow. The hybrid model A shows a distinctly different behavior at the same wind speed. Across the outer-span stations, the streamline patterns remain more coherent and better aligned, with reduced separation extent and a narrower wake, particularly near the tip region. The OA-T airfoil maintains flow attachment over a larger portion of the suction surface, indicating delayed separation and improved boundary-layer stability under high-loading conditions. This more streamlined outer-span flow organization is consistent with the steadier tangential aerodynamic loading and higher torque output observed for the hybrid rotor at elevated wind speeds. Under these conditions, the increased dynamic pressure intensifies the adverse pressure gradients along the blade, promoting separation in the baseline rotor. The OA-T modification alters the pressure distribution in the outer span, allowing the blade to maintain higher tangential aerodynamic loading near the tip under high inflow conditions.

3.4. Pressure-coefficient distributions and spanwise evolution

https://doi.org/10.5194/wes-2026-111
Preprint. Discussion started: 22 July 2026

To further clarify the aerodynamic mechanisms responsible for the performance differences between the baseline and hybrid model A rotors, sectional pressure-coefficient distributions C_p (x/c) were analyzed at the outer portion of the blade. The evolution of C_p (x/c) was examined at several spanwise locations, ranging from 70% to 95% span, encompassing our blade section, for wind speeds of 5, 10, and 15 m/s. Representative results at 85% and 95% span are discussed in the main text, while the complete set of sectional pressure-coefficient distributions across the 70–95% span range is provided in Appendix A. At U_∞=5 m/s, the baseline blade exhibits smooth and consistent sectional C_p loop distributions at both 85% and 95% span, with closely overlapping curves and a clear chordwise evolution from the leading-edge region toward gradual recovery near the trailing edge. This indicates a stable outer-span pressure field under low aerodynamic loading. In contrast, hybrid model A shows a noticeably different shape at the same spanwise stations: the sectional distribution contains a broader mid-chord area and exhibits small-amplitude fluctuations associated with laminar separation bubbles in the mid- to aft-chord region. These differences indicate that the OA-T outer-span modification alters the chordwise pressure recovery behavior even in the low-speed regime, while the overall loop remains coherent and consistent with the attached-flow operating condition suggested by the low-speed performance results. Moving to U_∞=10 m/s, the sectional pressure-coefficient loops reveal a clear transition toward higher aerodynamic loading. We notice that the hybrid model A exhibits a more structured evolution of the sectional pressure field at the same wind speed. Although a broader reduced pressure gradient at mid-chord region and small-scale fluctuations, are visible, the pressure-coefficient loops remain globally coherent and show reduced spanwise divergence between 85 % and 95 % span. This behavior suggests that the OA-T modification helps stabilize the outer-span pressure distribution under moderate aerodynamic loading, delaying the progressive loss of pressure recovery observed for the baseline configuration.

https://doi.org/10.5194/wes-2026-111
Preprint. Discussion started: 22 July 2026

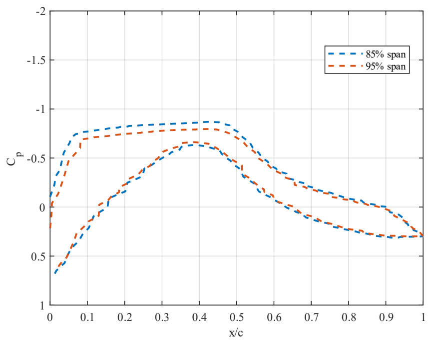

***Figure a** Baseline sectional pressure coefficient distributions Cp vs (x/c) at outer-span blade stations (85%, 95% span) for U∞=5 m/s*

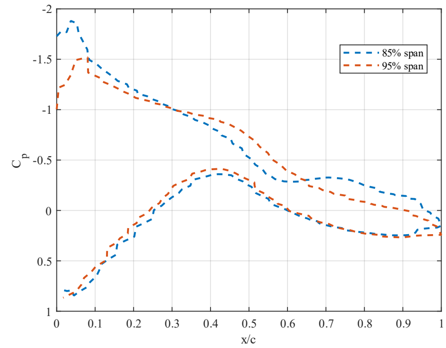

Figure b Baseline sectional pressure coefficient distributions Cp vs (x/c) at outer-span blade stations (85%, 95% span) for $U∞$=10 m/s

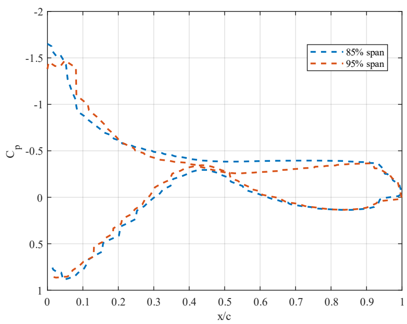

Figure c Sectional pressure coefficient distributions Cp vs (x/c) at outer-span of baseline blade stations (70–95% span) for $U∞$=15 m/s

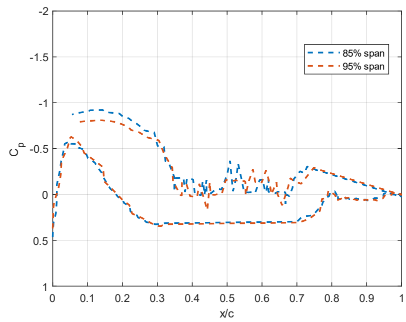

***Figure d** Model A sectional pressure coefficient distributions Cp vs (x/c) at outer-span blade stations (85%, 95% span) for U∞=5 m/s*

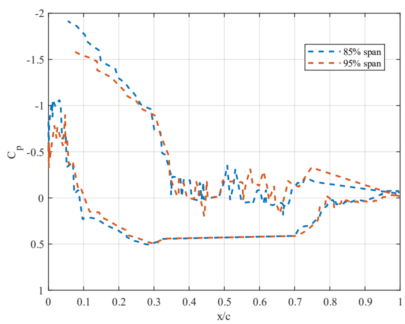

***Figure e** Model A sectional pressure coefficient distributions Cp vs (x/c) at outer-span blade stations (85%, 95% span) for U∞ =10 m/s*

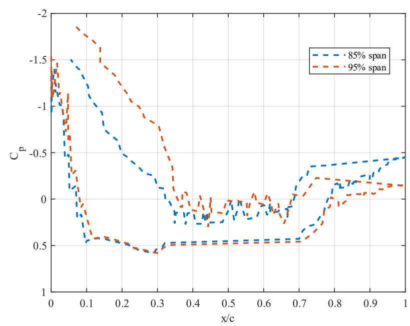

***Figure f** Model A sectional pressure coefficient distributions Cp vs (x/c) at outer-span blade stations (85%, 95% span) for U∞=15 m/s*

Figure 16 Outer-Span Sectional Pressure-Coefficient Distributions

https://doi.org/10.5194/wes-2026-111
Preprint. Discussion started: 22 July 2026

At 15 m/s, the differences become more pronounced. The baseline blade exhibits a stronger leading-edge suction peak near x/c≈ 0.1, indicating concentrated front-loading; however, beyond approximately x/c≈ 0.2, suction levels decrease more rapidly along the chord, and the pressure recovery becomes less uniform. Hybrid model A, by contrast, shows a weaker leading-edge peak but sustains a higher suction level over most of the chord (from roughly x/c≈ 0.2 to the trailing edge) at both 85 % and 95 % span. This reflects a redistribution of aerodynamic loading from a sharply front-loaded profile toward a more chordwise-distributed pressure field. Notably, the qualitative behavior of the hybrid configuration remains consistent across all investigated wind speeds, with the quasi-uniform distribution persisting as loading increases especially at suction side.

The spanwise distributions provided in **Appendix A and B** (70–95 % span), confirm that this behavior is not confined to a single section but characterizes the broader outer blade region. Overall, the pressure-coefficient analysis indicates that the OA-T modification appears to promote a more chordwise-distributed and spanwise-consistent pressure field in the outer span, particularly under moderate to high loading.

3.5. Three-Dimensional Flow Structures and Surface Loading Characteristics

3.5.1. Surface pressure contours and outer-span loading distribution

Surface pressure contours on the pressure and suction sides were examined for the baseline and hybrid model A blades at 5 and 15 m/s to visualize how the OA-T modification redistributes aerodynamic loading over the blade surface (**Fig 17 and 18)**.

At 5 m/s, the baseline blade shows a comparatively smooth pressure field along the outer span, with the pressure side exhibiting a gradual spanwise variation and the suction side maintaining a broad low-pressure region that extends over a larger portion of the chord. In contrast, hybrid model A displays a more structured pressure pattern in the outer-span modification region. A distinct high-pressure zone is retained over the modified outer section on the pressure side, consistent with the altered local curvature of the OA-T profile. On the suction side, the pressure drop toward the trailing edge appears more spatially confined than for the baseline blade, indicating a different chordwise pressure recovery behavior in the modified region even under low-loading conditions. At 15 m/s, the differences in pressure-field organization become more pronounced. For hybrid model A, the pressure side exhibits higher pressure levels with a more uniform distribution across a larger portion of the blade surface, indicating a more broadly distributed

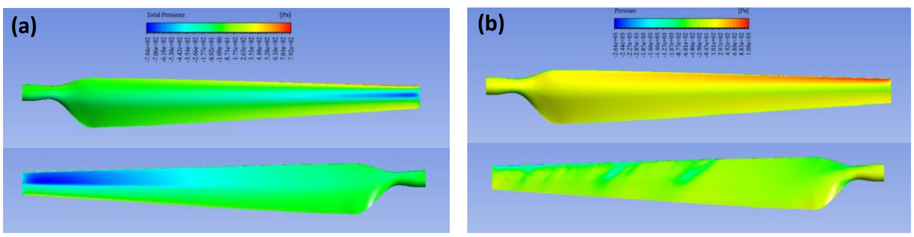

Figure. 17. Pressure contours on the NREL Phase VI blade pressure and suction side at (a) 5 m/s, and (b) 15 m/s

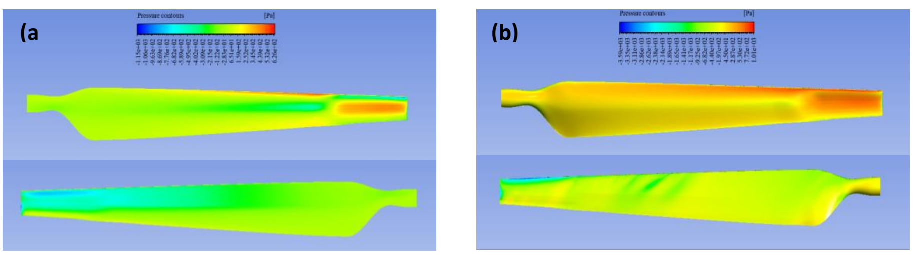

Figure. 18. **Pressure contours on the Hybrid Model A blade pressure and suction side at (a) 5 m/s, and (b) 15 m/s**

https://doi.org/10.5194/wes-2026-111
Preprint. Discussion started: 22 July 2026

loading state. Conversely, the baseline blade retains a more localized high-pressure concentration, most notably near the leading-edge outer-span region, indicating a more front-loaded pressure-side loading pattern under high wind speed. These surface-pressure trends are consistent with the sectional *Cp (x/c)* results, where the hybrid configuration exhibited a more sustained chordwise pressure plateau over much of the chord while the baseline showed stronger leading-edge loading. Overall, the surface pressure contours support the interpretation that the OA-T outer-span hybridization modifies the chordwise and spanwise distribution of pressure loading, with the effect becoming increasingly evident as wind speed increases.

3.5.2. Three-dimensional velocity streamlines

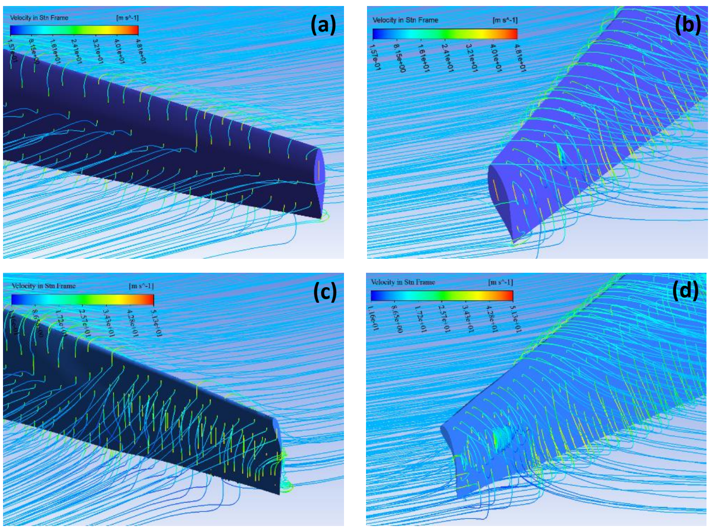

Figure .19 Three-dimensional velocity streamlines in the stationary frame at U∞=10 m/s for (a, b) baseline NREL Phase VI and (c, d) Hybrid Model A configurations.

Three-dimensional velocity streamlines in the stationary frame were examined at U_∞*=10 m/s* to assess wake development and outer-span flow organization under moderate aerodynamic loading (**Fig.19**). Representative oblique and side views are shown for both the baseline and hybrid model A configurations. We notice clear differences in outer-span flow organization between both models. In the near-tip oblique view, the baseline rotor exhibits stronger streamline curvature and more pronounced surface-adjacent distortion as the flow travels toward the trailing edge, particularly in the outer-span region. The associated wake structure downstream appears broader, with streamlines spreading more rapidly after leaving the blade tip. In contrast, hybrid model A maintains a more aligned streamline pattern along the blade surface, with reduced curvature and a visibly narrower wake development downstream. The tip vortex in the hybrid case appears more compact and coherent, with less lateral spreading in the immediate wake region. These differences indicate that the OA-T modification influences how outer-span loading is transferred into the wake, producing a more organized downstream flow structure compared to the baseline configuration under the same operating condition. The observed streamline organization is consistent with the previously identified redistribution of sectional pressure loading and improved torque retention at moderate wind speed.

3.5.3. **Turbulent Kinetic Energy Distribution**

The distribution of turbulent kinetic energy (*TKE*) was examined at U_∞=15 m/s to evaluate the turbulence footprint associated with outer-span loading (**Figs. 20, 21**). Representative results at 85 % and 95 % span are shown for both configurations. The contrast

https://doi.org/10.5194/wes-2026-111
Preprint. Discussion started: 22 July 2026

WIND ENERGY SCIENCE DISCUSSIONS

between the two configurations becomes more apparent, comparing it to lower wind speeds (See A**ppendix C).** The baseline rotor exhibits a broader region of

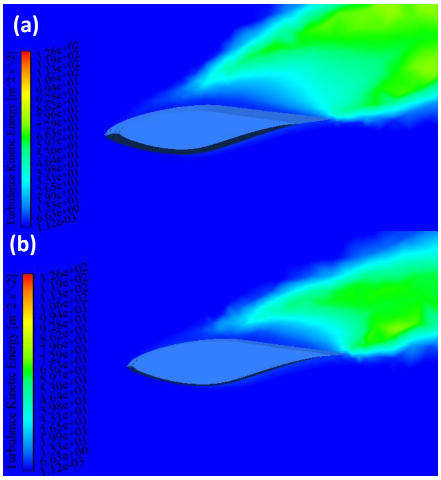

Fig. 20 Scattered Turbulence Kinetic Energy the NREL Phase VI blade at 15 m/s at locations (a) 85 %, (b) 95 %, span

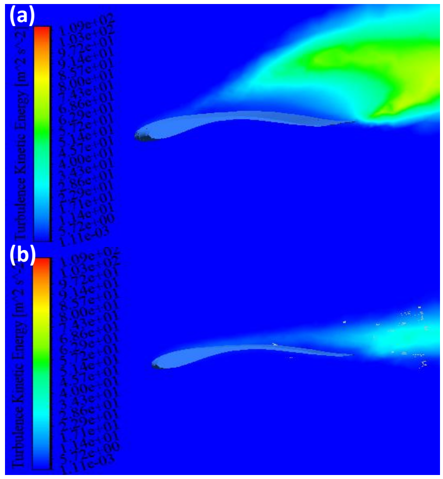

Fig. 21 Scattered Turbulence Kinetic Energy the Model A blade at 15 m/s at locations (a) 85 %, (b) 95 %, span

elevated turbulent kinetic energy extending from the outer-span suction side into the near wake, particularly at 95% span. The turbulence intensity spreads more diffusely downstream, indicating stronger mixing and a less confined wake structure. In comparison, hybrid model A shows a noticeably more compact *TKE* footprint. Although localized turbulence remains present near the trailing edge and tip region, the high-energy zones are spatially more contained and decay more rapidly into the wake. This more organized turbulence distribution aligns with the previously observed streamline coherence and chordwise pressure redistribution introduced by the OA-T modification. A more confined wake and reduced spread of high *TKE* regions suggest a more controlled tip region flow behavior under high loading. Since wake turbulence and vortex dynamics are commonly associated with broadband aerodynamic noise generation, this behavior could have favorable implications for acoustic performance. Quantifying this effect would require a dedicated aeroacoustic analysis, and it is a work under progress.

3.6. Integrated Aerodynamic Mechanism and Performance Implications

The global performance results and the detailed flow-field analyses show a consistent aerodynamic mechanism behind the behavior of hybrid model A. The OA-T outer-span modification modifies how pressure is distributed along the blade chord, replacing the increasingly front-loaded response observed in the baseline configuration with a more chordwise-distributed loading pattern characterized by a sustained mid-chord pressure plateau. This behavior is already visible at 5 m/s and remains consistent as wind speed increases, indicating that the hybrid modification changes the aerodynamic behavior of the outer span rather than simply shifting performance at a single operating condition. As loading intensifies toward 10 and 15 m/s, the baseline rotor exhibits sharper leading-edge pressure peaks, broader wake expansion, and more spatially extended turbulent kinetic energy regions, reflecting increased sensitivity of the outer blade region to elevated inflow angles. In contrast, hybrid model A maintains a more consistent outer-span flow patterns, with smoother pressure redistribution, improved streamline coherence near the tip, and a more confined turbulence footprint downstream. This redistribution moderates localized pressure gradients while preserving effective suction over a larger portion of the chord, thereby sustaining torque generation under higher wind speeds. The combined evidence from spanwise loading distributions, sectional *Cp (x/c)* evolution, surface pressure contours, wake organization, and *TKE* confinement indicates

https://doi.org/10.5194/wes-2026-111
Preprint. Discussion started: 22 July 2026

that the owl-inspired hybridization results in more stable aerodynamic loading in the outer blade region. Rather than relying on localized front-loading, the modified blade achieves a more stable and spatially distributed loading state, which translates into improved torque retention, higher power extraction at elevated wind speeds, and a more controlled wake development across the investigated operating range.

Conclusions

In this study we introduced and assessed an owl-inspired outer-span hybridization strategy for the NREL Phase VI rotor, where the OA-T airfoil was integrated in the tip region (Hybrid Model A) to improve aerodynamic performance and high-wind robustness. The numerical framework was first validated at two levels: (i) at the airfoil scale, the Transition *SST* model reproduced the overall experimental lift-curve trend of the owl-like airfoil, with only a small, explainable deviation around $\alpha \approx 4^{\circ}$- 6° consistent with the sensitivity of laminar separation-bubble dynamics reported in the reference experiments; and (ii) at the rotor scale, the baseline Phase VI torque–wind-speed response was captured with good agreement, including the rise in attached-flow conditions and the subsequent plateau/attenuation associated with stall onset. Using this validated setup without numerical retuning, the hybrid rotor demonstrated systematic aerodynamic gains: the peak power coefficient increased from $C_p = 0.38$ (baseline) to $C_p = 0.42$ at $\lambda = 5.41$, and further reached $C_p = 0.448$ at $\lambda = 7.58$, corresponding to an overall improvement of about 7–10% across the optimal operating range. These global gains were consistent with local evidence from spanwise tangential loading, which showed an outward redistribution of torque-producing contribution in the OA-T-modified region and a more stable loading behavior at high wind speed. Flow-field diagnostics provided a coherent physical explanation: sectional streamlines and chordwise pressure behavior indicated that the hybrid configuration consistently reorganizes outer-span loading by promoting a more chordwise-distributed pressure response (persistent Cp plateau behavior across speeds) rather than strongly front-loaded behavior, while 3D streamlines in the stationary frame at 10 m/s showed a more coherent near-tip wake and a more compact tip-vortex development for the hybrid rotor. At 15 m/s, the turbulent kinetic energy (*TKE*) fields further supported this trend, with a more confined turbulence footprint for hybrid model A compared with the broader, more diffused high-*TKE* region observed for the baseline rotor. Although no direct aeroacoustic computation was performed, the observed confinement of wake turbulence and reduced diffusion of high-*TKE* regions suggest potentially favorable implications for broadband aerodynamic noise mechanisms, which should be quantified in future dedicated aeroacoustic analyses. Overall, the results support the effectiveness of owl-inspired outer-span hybridization as a practical bio-inspired design route to enhance energy capture while improving the aerodynamic robustness of the tip region under increasing wind-speed loading.

Funding

The authors express their gratitude to the International University of rabat (UIR) and LERMA laboratory for providing the financial support to conduct this research.

Declaration of Competing Interest

The authors declare that they have no known competing financial interests or personal relationships that could have appeared to influence the work reported in this paper.

Data availability

The data supporting the findings of this study, including the numerical simulation data and post-processing results, are available from the corresponding author upon reasonable request. Additional information required to reproduce or further analyze the results presented in this paper will be provided where possible.

https://doi.org/10.5194/wes-2026-111
Preprint. Discussion started: 22 July 2026

Author contribution

Y.E.Q. conceived the study, developed the methodology, performed the numerical simulations, carried out the formal analysis, validated the results, prepared the visualizations, and wrote the original manuscript. K.Q. contributed to the methodology, validation, formal analysis, visualization, and the review and editing of the manuscript. A.A.O. contributed to the conceptualization and methodology of the study, supervised the research, and reviewed and edited the manuscript. W.L. contributed to the software development and reviewed and edited the manuscript. K.B. contributed to the investigation, provided resources, and reviewed and edited the manuscript. All authors discussed the results, contributed to the final version of the manuscript, and approved it for publication.

References

Aldheeb, M.A., Asrar, W., Sulaeman, E., Omar, A.A., 2016. A Review on Aerodynamics of Non-Flapping Bird Wings. J. Aerosp. Technol. Manag. 8, 7–17. https://doi.org/10.5028/jatm.v8i1.564
Anyoji, M., Wakui, S., Hamada, D., Aono, H., 2018. Experimental Study of Owl-Like Airfoil Aerodynamics at Low Reynolds Numbers. J. Flow Control Meas. Amp Vis. 06, 185–197. https://doi.org/10.4236/jfcmv.2018.63015
Aono, H., Kondo, K., Nonomura, T., Anyoji, M., Oyama, A., Fujii, K., Yamamoto, M., 2020. Aerodynamics of Owl-like Wing Model at Low Reynolds Numbers. Trans. Jpn. Soc. Aeronaut. SPACE Sci. 63, 8–17. https://doi.org/10.2322/tjsass.63.8
Ashraf, O., Adel, K., jetlawi, M., 6-9 june. Numerical Simulation of the Flapping Eagle, Owl and S1223 Airfoils. Presented at the Recent Advances in Air and Space Technologies (RAST2023) conference, Istanbul, Turkiye.
Boughou, S., Omar, A.A., Elsayed, O.A., Aldheeb, M., 2023. Numerical investigation on the aerodynamics of high-lift and bird-like low Reynolds number airfoils. Prog. Comput. Fluid Dyn. Int. J. 23, 146. https://doi.org/10.1504/PCFD.2023.131027
Burton, T., Jenkins, N., Sharpe, D., Bossanyi, E., 2011. Wind Energy Handbook, 1st ed. Wiley. https://doi.org/10.1002/9781119992714
Du, Z., Selig, M., 1998. A 3-D stall-delay model for horizontal axis wind turbine performance prediction, in: 1998 ASME Wind Energy Symposium. Presented at the 1998 ASME Wind Energy Symposium, American Institute of Aeronautics and Astronautics, Reno,NV,U.S.A. https://doi.org/10.2514/6.1998-21
El Qamch, Y., Bouchaala, K., Ali Omar, A., Lahmili, W., 2025. Biomimetic Airfoils in Wind Turbine Design: Innovations in Noise Mitigation and Aeroacoustic Performance Inspired by Avian Morphology. Sol. Energy Sustain. Dev. J. 14, 121–146. https://doi.org/10.51646/jsesd.v14i2.589
El Qamch Yassine, Bouchaala Kenza, Omar Ashraf A., Lahmili Wafae, 2025. Numerical Investigation of Thickness Variation on Owl-Like Airfoil Aerodynamics and Aeroacoustics at Low Reynolds Number. Acta Mech. Sin. https://doi.org/10.1007/s10409-025-25241-x
Geyer, T., Sarradj, E., Fritzsche, C., 2010. Measurement of the noise generation at the trailing edge of porous airfoils. Exp. Fluids 48, 291–308. https://doi.org/10.1007/s00348-009-0739-x
Hansen, M.O.L., 2015. Aerodynamics of Wind Turbines, 3rd ed. ed. Taylor & Francis Group, London.
Howe, M.S., 1991. Aerodynamic noise of a serrated trailing edge. J. Fluids Struct. 5, 33–45. https://doi.org/10.1016/0889-9746(91)80010-B
Jaworski, J.W., Peake, N., 2013. Aerodynamic noise from a poroelastic edge with implications for the silent flight of owls. J. Fluid Mech. 723, 456–479. https://doi.org/10.1017/jfm.2013.139
Johansen, J., Sørensen, N.N., 2004. Aerofoil characteristics from 3D CFD rotor computations. Wind Energy 7, 283–294. https://doi.org/10.1002/we.127
Kondo, K., Aono, H., Nonomura, T., Anyoji, M., Oyama, A., Liu, T., Fujii, K., Yamamoto, M., 2014. Analysis of Owl-like Airfoil Aerodynamics at Low Reynolds Number Flow. Trans. Jpn. Soc. Aeronaut. SPACE Sci. Aerosp. Technol. Jpn. 12, Tk_35-Tk_40. https://doi.org/10.2322/tastj.12.Tk_35
Lahmili, W., Bouchaala, K., Omar, A.A., El Qamch, Y., 2026. 2D Simulations on a Flat Plate to Study the Effect of a Single Cavity as a Step Toward Porosity-Based Skin Friction Drag Reduction, in: Cetin, B., Dursunkaya, Z., Günay, A.A., Gözükara, A.C. (Eds.), Advances in Computational Heat and Mass Transfer II, Lecture Notes in Mechanical Engineering. Springer Nature Switzerland, Cham, pp. 59–71. https://doi.org/10.1007/978-3-032-16135-2_6
Liu, T., Kuykendoll, K., Rhew, R., Jones, S., 2006. Avian Wing Geometry and Kinematics. AIAA J. 44, 954–963. https://doi.org/10.2514/1.16224
Menter, F.R., 1994. Two-equation eddy-viscosity turbulence models for engineering applications. AIAA J. 32, 1598–1605. https://doi.org/10.2514/3.12149
Omar, A., Rahuma, R., Emhemmed, A., 2020. Numerical Investigation on Aerodynamic Performance of Bird's Airfoils. J. Aerosp. Technol. Manag. e4620. https://doi.org/10.5028/jatm.v12.1182
Qaissi, K., Elsayed, O., Faqir, M., Essadiqi, E., 2023. Aerodynamic Optimization of Trailing-Edge-Serrations for a Wind Turbine Blade Using Taguchi Modified Additive Model. Energies 16, 1099. https://doi.org/10.3390/en16031099

https://doi.org/10.5194/wes-2026-111
Preprint. Discussion started: 22 July 2026

Qamch, Y.E., Omar, A.A., Qaissi, K., Lahmili, W., Bouchaala, K., 2026. Bio-Inspired Owl Airfoils for Improved Aerodynamic Performance of Small-Scale Wind Turbines. J. Phys. Conf. Ser. 3224, 042010. https://doi.org/10.1088/1742-6596/3224/4/042010
Rocha, P.A.C., Rocha, H.H.B., Carneiro, F.O.M., Vieira Da Silva, M.E., Bueno, A.V., 2014. k–ω SST (shear stress transport) turbulence model calibration: A case study on a small scale horizontal axis wind turbine. Energy 65, 412–418. https://doi.org/10.1016/j.energy.2013.11.050
Sørensen, J.N., 2011. Aerodynamic Aspects of Wind Energy Conversion. Annu. Rev. Fluid Mech. 43, 427–448. https://doi.org/10.1146/annurev-fluid-122109-160801

APPENDIX A: Figure A1: Outer-Span Sectional Pressure-Coefficient Distributions

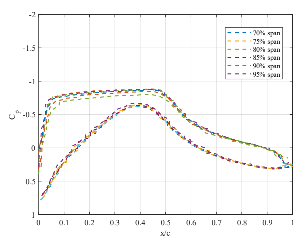

***Figure a** Sectional pressure coefficient distributions Cp vs (x/c) at outer-span of baseline blade stations (70–95% span) for $U\infty$=5 m/s*

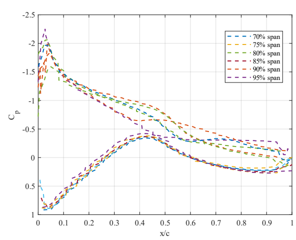

***Figure b** Sectional pressure coefficient distributions Cp vs (x/c) at outer-span of baseline blade stations (70–95% span) for $U\infty$=10 m/s*

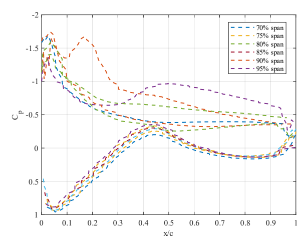

***Figure c** Sectional pressure coefficient distributions Cp vs (x/c) at outer-span of baseline blade stations (70–95% span) for $U\infty$=15 m/s*

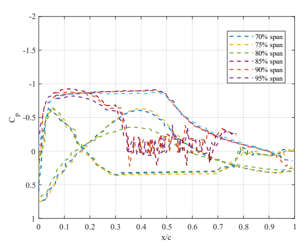

***Figure d** Sectional pressure coefficient distributions Cp vs (x/c) at outer-span of Model A blade stations (70–95% span) for $U\infty$=5 m/s*

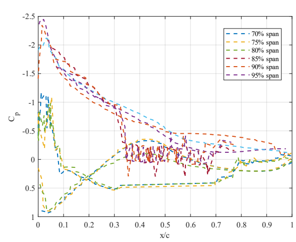

***Figure e** Sectional pressure coefficient distributions Cp vs (x/c) at outer-span of Model A blade stations (70–95% span) for $U\infty$=10 m/s*

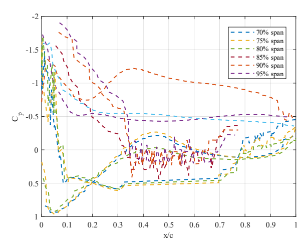

***Figure f** Sectional pressure coefficient distributions Cp vs (x/c) at outer-span of Model A blade stations (70–95% span) for $U\infty$=15 m/s*

Figure A2: Outer-Span Sectional Pressure Distributions

https://doi.org/10.5194/wes-2026-111
Preprint. Discussion started: 22 July 2026

eawe european academy of wind energy
Open Access WIND ENERGY SCIENCE DISCUSSIONS

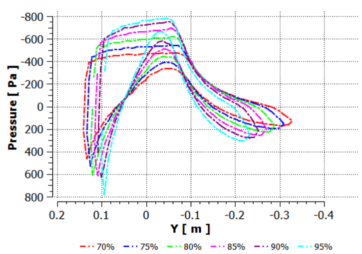

Figure a *Pressure distribution around the NREL Phase VI rotor blade sections at 70–95% span at 5m/s*

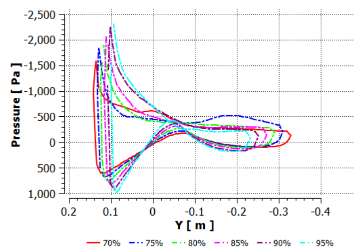

Figure b *Pressure distribution around the NREL Phase VI rotor blade sections at 70–95% span at 13m/s*

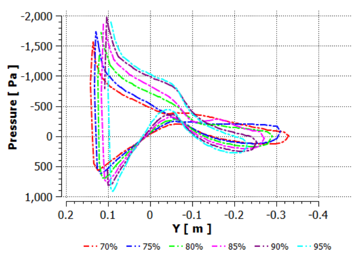

Figure c *Pressure distribution around the NREL Phase VI rotor blade sections at 70–95% span at 15m/s*

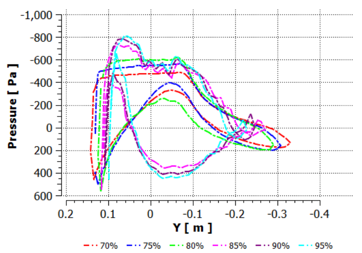

Figure d *Pressure distribution around the Model A rotor blade sections at 70–95% span at 5m/s*

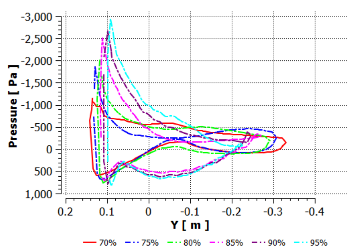

Figure e *Pressure distribution around the Model A rotor blade sections at 70–95% span at 13m/s*

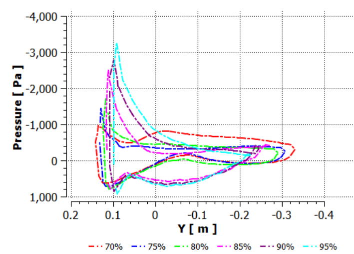

Figure f *Pressure distribution around the Model A rotor blade sections at 70–95% span at 15m/s*

Figure A3: Turbulent Kinetic Energy Distributions at Outer-Span Blade Stations (a) 70%, (b) 85%, (c) 90%, (d) 95% for Baseline and Hybrid Model A Rotors at U_∞=5 m/s

https://doi.org/10.5194/wes-2026-111
Preprint. Discussion started: 22 July 2026

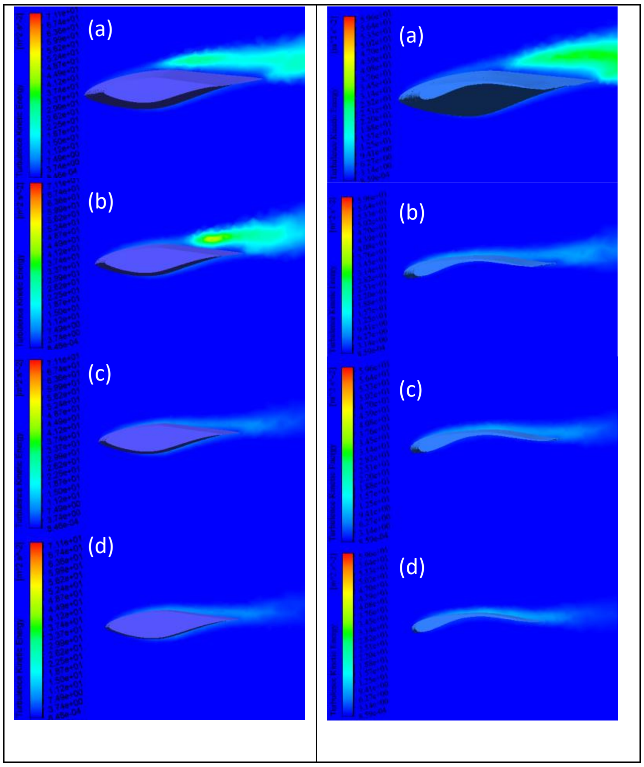

Table A1 : Baseline Blade Geometry Definition (NREL Phase VI)

r (m)	r/R	Chord (m)	Twist (deg)	Thickness (m or %c)	Twist Axis (%c)
0.508	0.092	0.218	0	0.218	50
0.66	0.12	0.218	0	0.218	50
0.883	0.16	0.183	0	0.183	50
1.008	0.183	0.349	6.7	0.163	35.9
1.067	0.193	0.441	9.9	0.154	33.5
1.133	0.205	0.544	13.4	0.154	31.9
1.257	0.227	0.737	20.04	0.154	30
1.343	0.243	0.728	18.074	20.95% c	30
1.51	0.273	0.711	14.292	20.95% c	30
1.648	0.298	0.697	11.909	20.95% c	30
1.952	0.353	0.666	7.979	20.95% c	30
2.257	0.408	0.636	5.308	20.95% c	30
2.343	0.424	0.627	4.715	20.95% c	30
2.562	0.463	0.605	3.425	20.95% c	30
2.867	0.518	0.574	2.083	20.95% c	30
3.172	0.573	0.543	1.15	20.95% c	30
3.185	0.576	0.542	1.115	20.95% c	30
3.476	0.628	0.512	0.494	20.95% c	30
3.781	0.683	0.482	-0.015	20.95% c	30
4.023	0.727	0.457	-0.381	20.95% c	30
4.086	0.739	0.451	-0.475	20.95% c	30
4.391	0.794	0.42	-0.92	20.95% c	30

https://doi.org/10.5194/wes-2026-111
Preprint. Discussion started: 22 July 2026

eawe european academy of wind energy
Open Access WIND ENERGY SCIENCE DISCUSSIONS

4.696	0.849	0.389	-1.352	20.95% c	30
4.78	0.864	0.381	-1.469	20.95% c	30
5	0.904	0.358	-1.775	20.95% c	30
5.305	0.959	0.328	-2.191	20.95% c	30
5.532	1	0.305	-2.5	20.95% c	30